JACS
JOURNAL OF THE AMERICAN CHEMICAL SOCIETY
pubs.acs.org/JACS
Article

Colloidal Multi-Dot Nanorods

Gryphon A. Drake, Logan P. Keating, Conan Huang, and Moonsub Shim*

Cite This: J. Am. Chem. Soc. 2024, 146, 9074–9083
Read Online
ACCESS | Metrics & More | Article Recommendations | Supporting Information

ABSTRACT: Colloidal nanorod heterostructures consisting of multiple quantum dots within a nanorod (*n*-DNRs, where *n* is the number of quantum dots within a nanorod) are synthesized with alternating segments of CdSe "dot" and CdS "rod" via solution heteroepitaxy. The reaction temperature, time dependent ripening, and asymmetry of the wurtzite lattice and the resulting anisotropy of surface ligand steric hindrance are exploited to vary the morphology of the growing quantum dot segments. The alternating CdSe and CdS growth steps can be easily repeated to increment the dot number in unidirectional or bidirectional growth regimes. As an initial exploration of electron occupation effects on their optical properties, asymmetric 2-DNRs consisting of two dots of different lengths and diameters are synthesized and are shown to exhibit a change in color and an unusual photoluminescence quantum yield increase upon photochemical doping.

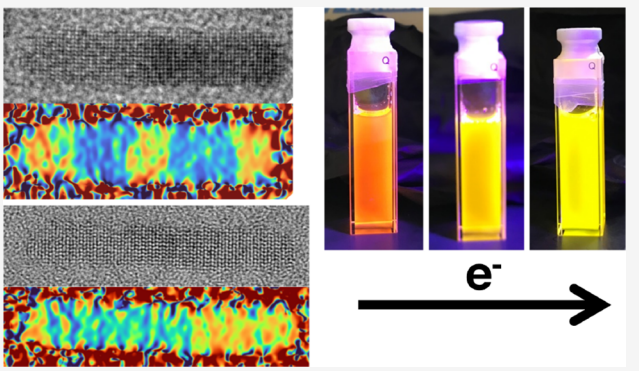

INTRODUCTION

Size-tunable optical properties of colloidal quantum dots (QDs) allow rapid advances in a variety of technologies, including fluorescent labels,[1] displays,[2−6] solar cells,[7−9] lasers,[10−12] and single-photon sources.[13,14] Various compositions and shapes are being explored, especially in the form of heterostructures, which broaden the engineering space for tailoring these materials for targeted applications. In particular, colloidal nanorod heterostructures, where smaller band gap QDs have been incorporated into a wider band gap rod, show much promise.[15] Composition[16−18] and strain[19−22] can impart a wider range of band gaps and therefore electronic and optical properties. Shapes with reduced symmetry can impart anisotropic properties and directionality for assembly.[23−28] Heterointerfaces can facilitate charge carrier manipulation. For example, efficient photoinduced charge separation,[29−34] two-photon upconversion at solar relevant fluxes,[35,36] and bidirectional light harvesting/emitting capability[37] have been demonstrated with heterostructures based on barbell-like nanorods.

A common feature enabling these materials is the controlled placement of size- and composition-tuned QDs within the nanorod. The ability to bring two QDs together with controlled spacing/barrier can lead to additional exciting effects including suppressed photoluminescence blinking and enhanced biexciton quantum yield[38] and local enhancement of the electric field.[39] Extending beyond the double-QD structures can lead to "molecules" of "artificial atoms" with tunable "bonds".[40−42] If the QDs are linked through crystalline, epitaxial spacers, their desirable properties (e.g., robustness and high photoluminescence quantum yield (PL QY)) may also be maintained.[43] Varying the number of QDs and the interaction between them may then lead to a multitude of new prospects.

The most straightforward multi-QD heterostructure is a linear system, where QDs are placed within a nanorod. We refer to these materials here as *n*-dot nanorods (*n*-DNRs), where *n* represents the number of QDs. Precise placement of multiple QDs of variable size and composition in *n*-DNRs can provide new paths to exploit band structure engineering concepts widely used in electronics and optoelectronics, from the double heterostructure that led to the realization of semiconductor lasers[44] to quantum well superlattices.[45] Achieving these linear "quantum dot molecules" through scalable solution synthesis will provide wide accessibility and versatility in processing.

The key requirements and challenges to the successful solution synthesis of *n*-DNRs include achieving high-quality epitaxial interfaces and controlling the number, size, and spacing of the QDs. There are many examples of defect-free heterointerfaces achieved through solution epitaxy on QDs and nanorods.[46−48] However, the latter need of controlling the number, size, and separation distance remains unexplored.

Received: December 13, 2023
Revised: February 19, 2024
Accepted: March 7, 2024
Published: March 22, 2024

https://doi.org/10.1021/jacs.3c14115
J. Am. Chem. Soc. 2024, 146, 9074−9083

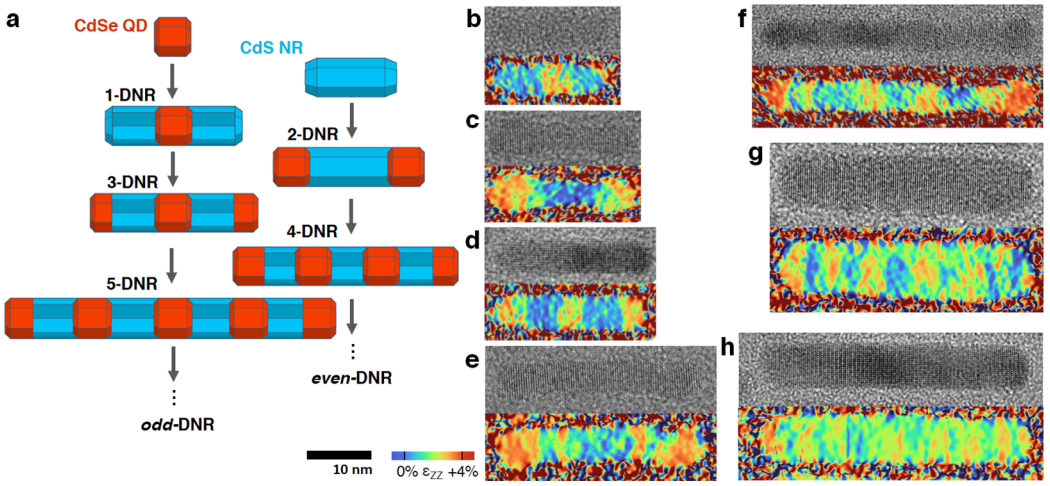

Figure 1. Schematic diagram of multidot nanorod (*n*-DNR) synthesis. (a) Starting from a CdSe QD or CdS nanorod, *n*-DNRs are synthesized via bidirectional growth. TEM micrographs and false-color Fourier-filtered axial distortion maps of exemplary CdSe/CdS *n*-DNRs with n = 1 (b), 2 (c), 3 (d), 4 (e), 5 (f), 7 (g), and 9 (h). The false color scale highlights CdSe regions with 4% greater wurtzite {0 0 0 1} lattice constant (orange) versus CdS (blue).

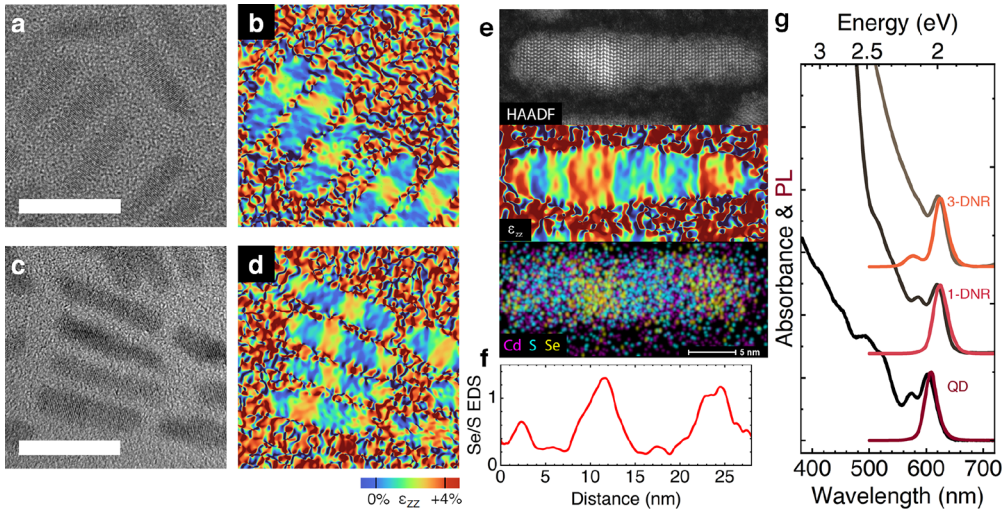

Figure 2. TEM micrographs and Fourier-filtered axial distortion maps of 1-DNRs (a, b) and bidirectionally grown 3-DNRs (c, d). (e) HAADF STEM image, Fourier-filtered axial distortion map, and Cd, S, and Se EDS map of a single 3-DNR. (f) Ratio of Se/S EDS intensity averaged across the particle diameter plotted along the particle length. (g) Absorption and PL spectra at each stage of bidirectional 3-DNR synthesis. Spectra are offset for the sake of clarity. The 3-DNRs exhibit two-color emission due to the tip CdSe segments being smaller than the central seed QD. Scale bars in (a) and (c) are 20 nm.

Directionality or regioselectivity in solution heteroepitaxy (e.g., unidirectional vs bidirectional tip growth) is also an important capability necessary for precision synthesis of *n*-DNRs. Here, we demonstrate a simple approach that combines and builds on rod growth on QDs and selective tip growth on nanorods established in dot-in-rods[24,49,50] and barbell-shaped nanorods,[16,51] respectively, to obtain *n*-DNRs via unidirectional and bidirectional solution heteroepitaxy. We focus on controlling the number and aspect ratio of QDs in *n*-DNRs and observe an interesting color change and PL QY increase upon photochemical doping in 2-DNRs.

RESULTS AND DISCUSSION

The two potential approaches to *n*-DNR synthesis developed here, unidirectional and bidirectional growth, focus on controlling the number, size, and shape of CdSe QDs within CdS nanorods. The bidirectional growth approach, where two QDs are grown at a time on the opposite ends of the seed nanorods, is a relatively straightforward extension of dot-in-rod and barbell-shaped nanorod syntheses. Unidirectional growth can provide a more delicate control over the size, shape, and spacing, one QD at a time, but requires overcoming the challenge of selective suppression of growth at one end of the nanorod. We first discuss controlling the number of QDs in bidirectional growth and how the tip morphology can be varied. We then explore how unidirectional growth can be achieved. Initial studies to examine how electron injection by photochemical doping affects their optical properties reveal an interesting and potentially useful color change with enhanced PL in 2-DNRs.

Bidirectional Growth. Barbell-shaped nanorods are obtained through QD growth at both tips of the nanorod seeds. For example, CdSe QDs can be grown on the tips of CdS nanorods.[51] Conversely, dot-in-rods are synthesized by a

https://doi.org/10.1021/jacs.3c14115
J. Am. Chem. Soc. 2024, 146, 9074−9083

"seeded" growth approach where CdS rods are grown on CdSe QDs.[24,49] By a combination of the two approaches, *n*-DNRs of an arbitrary number of QDs can be achieved. That is, starting with CdS rods, alternating CdSe dot and CdS rod growth at the tips will result in even-numbered *n*-DNRs. Alternating dot/rod growth starting from dot-in-rods, which can also be considered and will be referred to hereafter as 1-DNRs, will result in odd-numbered *n*-DNRs. A schematic of this combined approach along with examples of several different *n*-DNRs achieved in this manner are shown in Figure 1. One of the key challenges is ensuring that the reaction conditions for each growth step are compatible with and preserve the shape of the product from the prior step. As *n* increases, the structure may become increasingly more delicate, adding to the severity of the problem.

Starting from either a CdS nanorod or 1-DNR growth solution with excess Cd precursors, the dropwise addition of trioctylphosphine selenide (TOPSe) under a milder condition (250 °C) leads to CdSe tip growth. Additional CdS segments are then grown by dropwise addition of trioctylphosphine sulfide (TOPS) at a higher reaction temperature of 350 °C. The higher temperature needed for this step also leads to ripening that lowers the aspect ratio of CdSe tips, which were initially rod-shaped. While this ripening poses a potential problem in *n*-DNR synthesis, it can also be exploited to control the tip morphology or be circumvented by minimizing high-temperature exposure time before CdS growth as discussed later. The number of cycles of these alternating CdSe and CdS growth steps determines the number of QDs in the *n*-DNRs. These alternating growth steps can be carried out in a single pot or in multiple pots with purification after each CdS/CdSe growth cycle, the details of which are described in the Supporting Information. Examples of *n*-DNRs with *n* = 1, 2, 3, 4, 5, 7, and 9 are show in Figure 1b−h. High-resolution TEM images along with corresponding Fourier-filtered maps of relative lattice spacing that change with respect to the CdS lattice along the rod axis (referred hereon as axial distortion maps) are shown for these *n*-DNRs. With ∼4% lattice mismatch along the wurtzite *c* axis (ϵ_{zz}) between CdSe and CdS, the larger lattice CdSe QDs can be readily located within the nanorods through this analysis. The spacing between QDs in these *n*-DNRs can be varied by the amount of TOPS added for each rod growth step. The examples shown in Figure 1 are synthesized using amounts of TOPS and TOPSe, which result in CdS and CdSe segments of similar volume.

Figure 2 shows how the structure and optical properties evolve during *n*-DNR synthesis, for the example of 3-DNRs. In Figure 2a,b, a TEM image and the corresponding axial distortion map of an aliquot taken after the first CdS tip growth on seed CdSe QDs during 3-DNR synthesis are shown. The starting CdSe QDs have an average diameter of 4.7 nm with a narrow size distribution (±0.4 nm standard deviation), as the TEM images and the corresponding size histogram show (Supporting Information, Figure S1a,b). The growth of CdS on the seed CdSe QDs leads to the expected rod growth, resulting in 1-DNRs with less than 1 nm increase in the average diameter and average elongation more than three times the seed QD diameter for this particular case. The size distribution, as shown by the low-magnification TEM image and the size histogram (Supporting Information, Figure S1c,d), remains relatively narrow (average length = 16 ± 2 nm), typical of dot-in-rod growth. Subsequent bidirectional growth of CdSe at the tips, leading to two additional QDs, can be seen in the TEM image and the corresponding axial distortion map shown in Figure 2c,d. In this case, the QDs grown at the tips exhibit a smaller diameter than the seed QD in the center of the nanorod, which is achieved by the addition of less TOPSe. As indicated by the TEM image and histogram (Supporting Information, Figure S1e,f), the smaller QD tips lead to a small reduction in the average diameter from 5.5 to 5.1 nm and an increase in the average length of ∼4 nm while their distribution remains similar to the 1-DNR intermediate (3-DNR average length = 20 ± 3 nm). These results indicate that *n*-DNRs with higher *n* may be achieved without introducing a significant broadening in size distribution.

While the axial distortion maps, such as those shown in Figures 1 and 2b,d, can allow direct and rapid identification of CdSe and CdS segments from routine high-resolution TEM images, they rely on lattice spacing differences, which can be complicated by potential axial lattice strain. To verify that such effects do not complicate spatial identification of composition and to provide a more comprehensive characterization for the CdSe/CdS *n*-DNRs, high-angle annular dark field scanning transmission electron microscopy (HAADF STEM) and energy-dispersive X-ray spectroscopy (EDS) images are compared to the axial distortion map for a 3-DNR in Figure 2e. In the HAADF STEM image (Figure 2e, top), the central CdSe QD can be identified by higher contrast due to its larger size, but the QDs at the tips are difficult to distinguish. Stacking faults are observed at the central CdSe/CdS interface, as expected for relatively large core sizes.[52] The axial distortion and EDS maps, on the other hand, are able to distinguish both the central and tip CdSe QDs from CdS segments (Figure 2e, middle and bottom) with excellent agreement between the two methods. The axial profile of the Se/S ratio averaged across the rod diameter from the EDS map is shown in Figure 2f, and the locations of high Se signal regions agree very well with CdSe regions visualized in the axial distortion image.

Figure 2g shows the evolution of the UV−vis absorption and PL spectra as QDs are converted to 1-DNRs and then to 3-DNRs. The narrow absorption and emission features of the seed QDs are maintained upon CdS rod growth to 1-DNRs consistent with the observed size distributions seen in the TEM histograms (Supporting Information, Figure S1). The sharp increase in the optical density for photon energy >2.5 eV (<496 nm) is indicative of the CdS rod growth. The PL peak fwhm for seed QDs is 90 meV (27 nm), while that of the 1-DNRs is 96 meV (30 nm). The band edge absorption and PL redshift (PL peak maximum shifts from 2.04 eV nm to 1.98 eV) as expected due to CdSe and CdS forming a quasi-type II heterojunction in dot-in-rods.[24,46] The growth of smaller CdSe QDs at the tips leads to an increase in the optical density for energies >2.1 eV (<590 nm), arising from optical transitions in the smaller CdSe tips. This increase in the optical density is accompanied by a new PL feature at ∼2.15 eV (577 nm). The initial PL corresponding to the central QD remains unaltered with the same peak position of 1.98 eV (625 nm) and fwhm of 90 meV (29 nm). The evolution of PL excitation (PLE) and absorptance spectra for this synthesis series from QDs to 3-DNRs are shown in the Supporting Information, Figure S2. In addition to the difference in PLE and absorptance arising in the CdS absorption spectral region due to nonunity exciton localization efficiency as seen in 1-DNRs,[53] additional discrepancies are seen in the tip CdSe QD spectral region in the 3-DNR spectra. Given the distinct dual-peaked PL and the

https://doi.org/10.1021/jacs.3c14115
J. Am. Chem. Soc. 2024, 146, 9074−9083

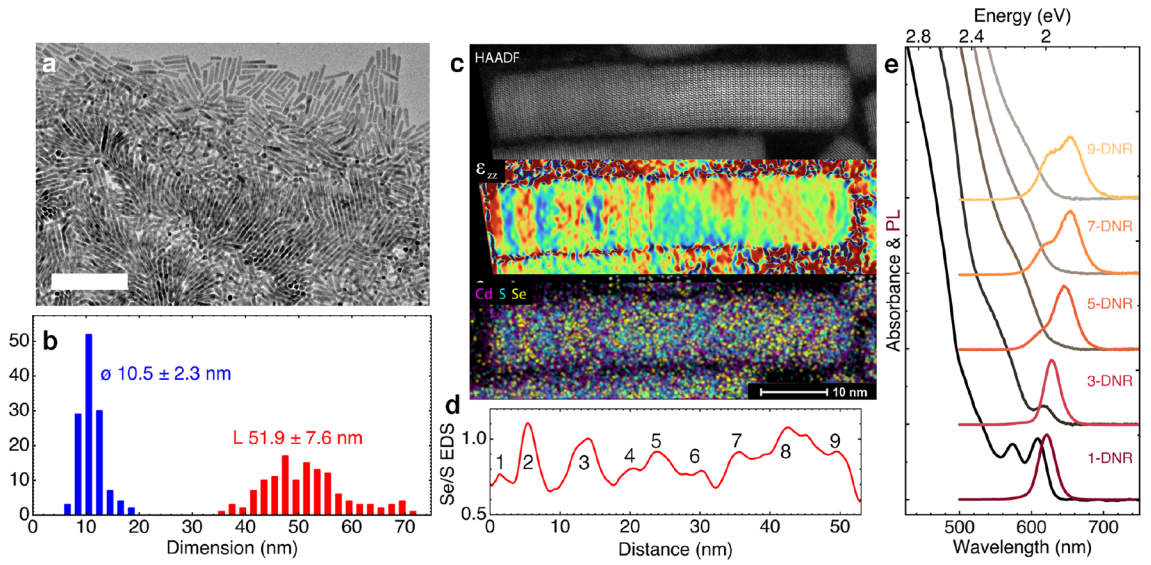

Figure 3. Low-magnification TEM micrograph (a) and size histogram (b) of CdSe/CdS 9-DNRs. (c) HAADF STEM image, Fourier-filtered axial distortion map, and Cd, S, and Se EDS map of a single bidirectionally grown CdSe/CdS/CdSe 9-DNR. (d) Ratio of Se/S EDS intensity averaged across the particle diameter plotted along the particle length with labeled peaks indicating the nine CdSe dot locations. (e) Absorption and PL spectra at different stages of 9-DNR synthesis. Spectra are offset for clarity. The scale bar in (a) is 200 nm.

PLE being detected at the redder PL peak, such a discrepancy may be expected.

The bidirectional growth approach can be extended, in principle, to an arbitrary number of QDs. Figure 3 demonstrates the feasibility with an example of 9-DNRs grown in a single pot starting from CdSe QD seeds. The low-magnification TEM image in Figure 3a shows local alignment of the rods comparable to 1-DNRs[54] and even close-packing that leads to rods standing up upon drying on the TEM grid, indicating that the narrow size distribution can be well maintained through four double-tip growth steps. The average diameter and length of the final 9-DNRs are 11 ± 2 and 52 ± 8 nm, respectively, as shown in the histogram in Figure 3b. The standard deviations of these dimensions are comparable to or only slightly larger than typical CdS single-phase nanorods and 1-DNRs. Figure 3c compares the HAADF STEM image with the corresponding axial distortion and EDS maps of a 9-DNR. While the multiple segments can be seen in the axial distortion map, identification of all 9 QDs in 9-DNRs can be difficult, especially in the case where the spacing between QDs is small and both components may be strained. In addition to the extension of the rod tips, a slight radial growth of CdS can occur, resulting in a more significant shell of CdS surrounding the central dot in higher *n*-DNRs with multiple tip growth steps. Axial compression of the central CdSe segments and increased S presence therefore make distortion and EDS mapping more difficult in identifying dot location and number in these structures. Nevertheless, the combination of the axial distortion map and axial profile of the Se/S ratio averaged across the rod diameter from the EDS map (Figure 3d) allows the identification of all 9 QDs in this 9-DNR.

The spectral evolution at each double-tip growth step of 9-DNRs is shown in Figure 3e. In the absorption spectra, the onset of the tip QDs can be seen at energy >2.1 eV (<590 nm) and continue to grow with each tip growth step. The smaller size of the tip QDs also leads to a second peak in the PL which grows in intensity and line width and slightly redshifts with each growth step. Figure S3 shows the evolution of PLE spectra compared to the corresponding absorptance spectra for this 9-DNR synthesis sequence. Similar to the 3-DNR case discussed above, the initial 1-DNR growth step leads to discrepancy starting at the onset of absorption of CdS. Upon the first tip growth to 3-DNR, the difference between PLE and absorptance extends into the red, where the tip CdSe QDs are expected to absorb. Compared to the 3-DNRs of Figure S2, there is a larger difference due to more absorption arising from large tip QDs in this case. Continued tip growth steps lead to a reduction in this PLE/absorptance discrepancy due to the electron energy levels of QDs becoming closer, as indicated by overlapping PL peaks. Further optimization to minimize the size distribution of each tip growth step is necessary for fine control over PL features, especially in *n*-DNRs with large *n*. Hence, it is important to understand how tip morphology is affected by the growth condition, which often leads to tips being smaller than the initial rod diameter.

Tip Morphology. The key reason for the growth of smaller CdSe tips is the tapering shape of wurtzite nanoparticles.[55−57] This tapering, when it occurs during growth, has been shown to lead to dual-diameter CdSe nanorods,[58] CdS nanorods, and 1-DNRs.[49,59] In the case of *n*-DNRs, we observe that tapering is often prominent after each CdS growth step. We suspect that the duration of exposure of the CdS-terminated intermediate of *n*-DNRs to an elevated reaction temperature prior to TOPSe addition makes them prone to tapering. That is, annealing at elevated temperature facilitates tapering that replaces the anion-terminated $(0\,0\,0\,\bar{1})$ facet with energetically more favorable $\{1\,\bar{1}\,0\,\bar{1}\}$ facets. The tapered CdS tip then leads to a smaller terminating $(0\,0\,0\,\bar{1})$ facet, upon which heterogeneous nucleation of CdSe occurs, resulting in a smaller diameter CdSe tip. In addition, because the presence of phosphonic acids promotes growth along the rod axis, the resulting CdSe tips can assume a high aspect ratio. On the opposite end, the $(0\,0\,0\,1)$ facet is less prone to this tapering effect since it is cation terminated in an environment with ligands that preferentially bind to cations and therefore is energetically stable compared to the $\{1\,\bar{1}\,0\,1\}$ slanted facets.[60]

https://doi.org/10.1021/jacs.3c14115
J. Am. Chem. Soc. 2024, 146, 9074−9083

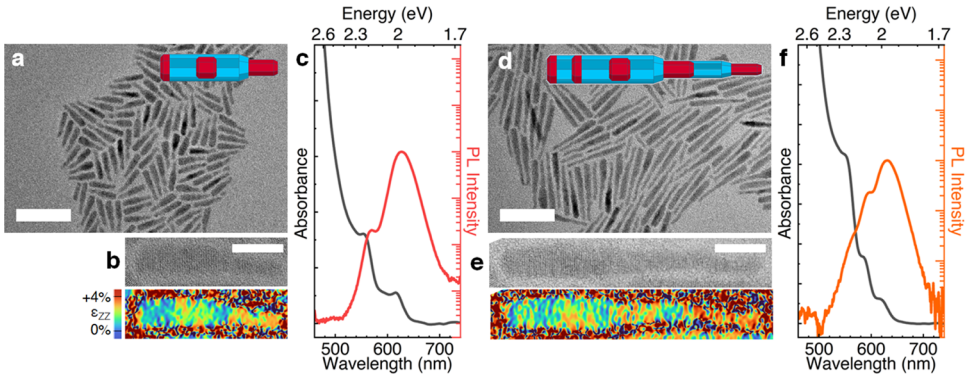

Figure 4. Low-magnification TEM micrograph (a), high-magnification TEM micrograph and Fourier-filtered axial distortion map (b), and absorption and semilogarithmic scale PL spectra (c) of asymmetric bidirectionally grown CdSe/CdS 3-DNRs. Low-magnification TEM micrograph (d), high-magnification TEM micrograph and Fourier-filtered axial distortion map (e), and absorption and semilogarithmic scale PL spectra (f) of asymmetric bidirectionally grown CdSe/CdS 5-DNRs. Inset diagrams in (a) and (d) schematically depict the corresponding *n*-DNRs with CdSe (red) and CdS (blue) segments indicated in different colors. Scale bars are 50 nm in (a) and (d) and 10 nm in (b) and (e).

An example illustrating the consequence of this tapering effect is shown for the case of 5-DNRs in Figure 4. For the 3-DNR step (Figure 4a), the larger diameter segment corresponds to the 1-DNR seed and the smaller diameter segment is the CdSe tip grown at the tapered $(0\ 0\ 0\ \bar{1})$ tip. A high-resolution TEM image and the corresponding axial distortion map are shown in Figure 4b to highlight the diameter modulation and spatial identification of the CdSe segments. The PL spectrum of an aliquot taken at the 3-DNR stage reveals a double-peaked emission, as expected due to the diameter modulation arising from the CdS tapering effect (Figure 4c). After the second CdSe tip growth step, three distinct diameter regions can be identified along 5-DNRs (Figure 4d,e). The diameter of the first CdSe $(0\ 0\ 0\ \bar{1})$ tip growth region increases slightly but remains smaller than that of the original seed CdSe region and larger than that of the final CdSe tip region. Evidently, the initial diameter of CdS segments growing along the $\langle 0\ 0\ 0\ \bar{1}\rangle$ direction closely matches that of the parent CdSe segment, which we interpret as a consequence of the elevated growth temperature enabling heteroepitaxy of CdS on CdSe $\{1\ \bar{1}\ 0\ \bar{1}\}$. The distinctly sized CdSe segments lead to three PL features in the resulting 5-DNRs (Figure 4f).

The diameter variation due to the tapering effect is an interesting consequence of the differences in the energies of the terminating facets and presents a potential path to the controlled modulation of size and shape in *n*-DNRs. In Figure 5, we demonstrate such an approach where the tip morphology of *n*-DNRs is varied with easily accessible reaction parameters such as reagent concentration and temperature. When CdSe tips are grown at the ends of the CdS segment at a lower temperature of 250 °C, they typically grow asymmetrically, with the CdSe grown on the $(0\ 0\ 0\ \bar{1})$ end being smaller in diameter and elongated (Figure 5a,b) due to the tapering effect in CdS nanorods discussed above. The corresponding absorption and PL spectra are shown in Figure 5c with the onset of absorption and an additional peak at ~2.4 eV (516 nm) due to the new smaller diameter CdSe segment. A larger amount of TOPSe added at the same reaction temperature of 250 °C leads to longer CdSe tips with a slight increase in the diameter (Figure 5d,e), which is accompanied by red-shifted absorption and PL features at ~2.25 eV (550 nm) (Figure 5f). When the reaction temperature is increased to 350 °C, the newly grown CdSe segments ripen to low aspect ratio tips, as

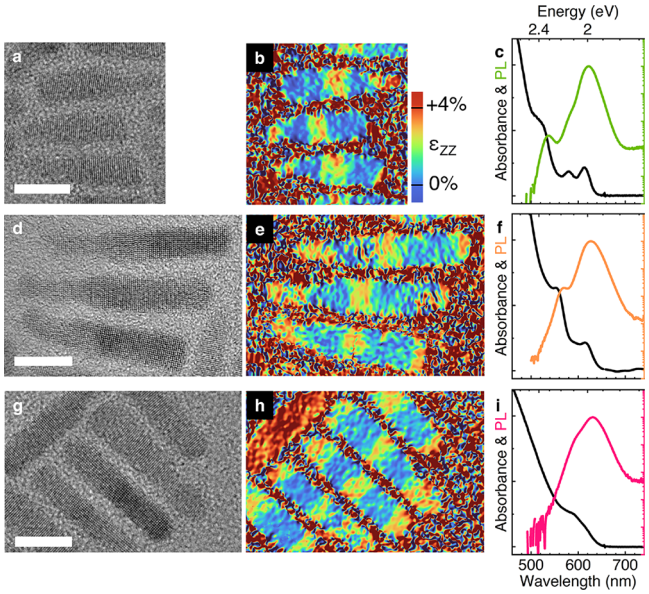

Figure 5. High-resolution TEM micrographs, Fourier-filtered axial distortion maps, and absorption and semilogarithmic scale PL spectra of bidirectionally grown CdSe/CdS 3-DNRs under different conditions. At 250 °C, growth of high aspect ratio CdSe occurs along $\langle 0\ 0\ 0\ \bar{1}\rangle$ from short (a–c) to long (d–f) as more TOPSe is supplied. Annealing at 350 °C results in nearly symmetric CdSe tips (g–i). The false color scale in (b), (e), and (h) highlights CdSe regions with 4% greater wurtzite $\{0\ 0\ 0\ 1\}$ lattice constant (orange) versus CdS (blue). Scale bars are 10 nm.

shown in Figure 5g,h. The corresponding spectral redshift leads to overlapping spectral features with those of the original seed QD at the center, giving rise to a broad shoulder in the band edge absorption and a nearly single-peaked PL (Figure 5i). This narrowing of the PL feature can be easily achieved in the single-pot synthesis, where the growing *n*-DNRs are kept at high reaction temperature for a longer period of time between each tip QD growth, causing CdSe segments to develop a low aspect ratio.

The high aspect ratio CdSe tips can be maintained if exposure to the higher CdS growth temperature is minimized. For this purpose, a multipot approach can be taken. Here, after each CdSe tip growth step at 250 °C, the *n*-DNRs are cooled and purified. These seed *n*-DNRs are then dissolved in TOP

https://doi.org/10.1021/jacs.3c14115
J. Am. Chem. Soc. 2024, 146, 9074–9083

along with TOPS and injected into Cd-alkyl phosphonate solution in TOPO at 350 °C. The ripening of previously grown CdSe tips is then minimized as CdS extensions grow immediately following the injection. Additional high aspect ratio CdSe tips can then be grown at 250 °C, and the process can be repeated for higher *n*-DNRs with elongated CdSe segments. Note that the 5-DNRs shown in Figure 4 were grown in this manner (synthesis details are given in the Supporting Information). Hence, the combination of the single- vs multipot strategy and the amount of Se reagent added provides a feasible and simple approach to varying the CdSe tip aspect ratio and volume, respectively.

Unidirectional Growth. While the asymmetric tips resulting from the bidirectional growth approach afford some control over the morphology of QDs in *n*-DNRs, ultimately, tailoring the size and shape of each QD independently would be ideal. One of the key reagents for selective tip growth is the alkyl phosphonic acid, which helps to differentiate growth rates along different crystallographic directions. Phosphonic acid ligands promote heteroepitaxy on $(0\ 0\ 0\ 1)$ and $(0\ 0\ 0\ \bar{1})$ tip facets while minimizing growth on $\{1\ \bar{1}\ 0\ 0\}$ side facets, resulting in the rod shape. However, the growth rates on the two tip facets, in general, are not the same. These rates have been suggested to be strongly affected by the surface-capping ligand choice. In particular, varying the ratio of octadecylphosphonic acid (ODPA) to hexylphosphonic acid (HPA) has been shown to differentiate $(0\ 0\ 0\ 1)$ vs $(0\ 0\ 0\ \bar{1})$ tip growth rates, with higher ODPA fraction increasing the relative growth rate along the $\langle 0\ 0\ 0\ \bar{1}\rangle$ direction.[49] By exploiting this effect, unidirectional growth of *n*-DNRs can be achieved with ODPA as the exclusive phosphonic acid ligand using the aforementioned multipot approach. The results are demonstrated in Figure 6. The spectral evolution during each step of the

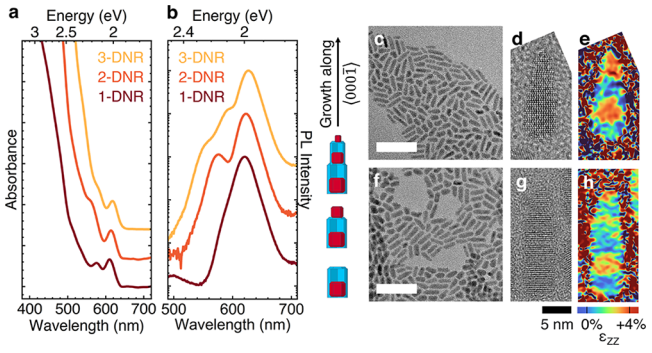

Figure 6. Absorption (a) and semilogarithmic scale PL (b) spectra of tapering CdSe/CdS 3-DNRs over the course of unidirectional growth. Spectra are offset for clarity. The diagram to the right of the spectra illustrates CdS (blue) and CdSe (red) segments growing along the wurtzite $\langle 0\ 0\ 0\ \bar{1}\rangle$ direction. Low- and high-magnification TEM images and false-color Fourier-filtered axial distortion maps of tapering 2-DNRs (c–e) and tapering 3-DNRs (f–h). The false color scale in (d) and (g) highlights CdSe regions with a larger lattice constant (orange) versus CdS (blue). Scale bars in (c) and (f) are 50 nm.

unidirectional growth of 3-DNRs is shown in Figure 6a,b. The growth of the initial CdS segment to 1-DNR causes redshifts in both the absorption and PL of the initial seed QDs as expected. Upon single CdSe tip growth, an absorption shoulder and a second PL peak at ∼2.2 eV (564 nm) appear, corresponding to the second QD, while the absorption and PL features of the original seed QD remain nearly unchanged. Low (Figure 6c) and high (Figure 6d) resolution TEM images of the 2-DNRs confirm the smaller diameter of the growing tip. The axial distortion map (Figure 6e) of the high-resolution TEM image reveals that the growth is unidirectional.

The final 3-DNRs exhibit a further increase in the absorption at >2.2 eV (<564 nm), corresponding to additional smaller CdSe growth, and the PL now exhibits three distinct features, with the weakest third one appearing at ∼2.25 eV (552 nm). Similar to the 2-DNR intermediate, the TEM images (Figure 6f,g) show decreasing diameter on one end but with increased length, and the axial distortion map (Figure 6h) indicates that the final QD has the smallest diameter. Similar to the bidirectional growth of 5-DNRs discussed earlier, the diameters of the second and the third QDs were maintained to be smaller through the multipot approach that minimizes ripening of CdSe tips at each step.

As established earlier for bidirectional growth, the diameter of growing QDs can be varied through CdS tapering and CdSe ripening effects, while the amounts of reagents added can determine the spacing and the overall volume of the QDs in *n*-DNRs. As an example of tailoring CdSe segment dimensions in the unidirectional growth regime, we have synthesized 2-DNRs with different CdSe bandgaps and segment volumes. The results are shown in Figure 7. The growth of the CdS rod and

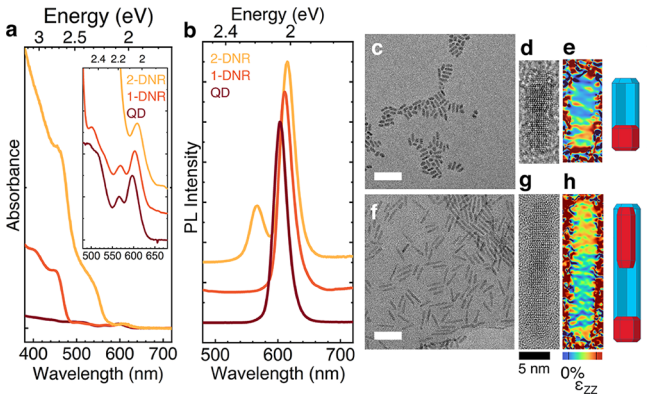

Figure 7. Absorption spectra (a) and PL spectra (b) of 2-DNRs over the course of unidirectional growth. The inset (a) shows the CdSe bandgap region. Spectra are offset for clarity. Low- and high-magnification TEM images and false-color Fourier-filtered axial distortion maps of 1-DNRs (c–e) and 2-DNRs (f–h). Diagrams to the right illustrate CdS (blue) and CdSe (red) segments growing along the $\langle 0\ 0\ 0\ \bar{1}\rangle$ direction. Scale bars in (c) and (f) are 50 nm.

CdSe tip segment on the CdSe QD seed is indicated in Figure 7a by the appearance of additional absorption peaks at ∼2.7 (459) and ∼2.3 eV (539 nm), respectively. Notably, the more quantum-confined CdSe segment is the more voluminous, as evidenced by its high absorption cross section relative to the core (Figure 7a) and more pronounced PL at 2.2 eV (Figure 7b).

As in the previous example, growth of CdS is essentially limited to the $\langle 0\ 0\ 0\ \bar{1}\rangle$ direction, with the initial seed CdSe dot being positioned at the $\langle 0\ 0\ 0\ 1\rangle$ tip (Figure 7c–e). Subsequently, a high aspect ratio CdSe segment is grown along $\langle 0\ 0\ 0\ \bar{1}\rangle$, followed by a thin shell of CdS (see the Supporting Information for details), resulting in 2-DNRs with two distinct CdSe tips (Figure 7f–h). In Figure 7h, the bottom tip corresponds to the initial spherical CdSe seed, while the top

https://doi.org/10.1021/jacs.3c14115
J. Am. Chem. Soc. 2024, 146, 9074–9083

corresponds to the higher-band gap CdSe segment. As quantum confinement is largely dependent on the smallest segment dimension (the diameter in this case), the length can be varied to increase the corresponding absorption cross section and relative PL intensity. For comparison, this 2-DNR exhibits higher energy PL intensity that is about 30% of the lower energy PL, whereas the 2-DNR shown in Figure 6b, where the more quantum-confined CdSe segment is the smaller volume, exhibits only about 10% for the higher energy PL.

Photochemical Doping. In order to explore the effects of electron occupation on the optical properties of these multidot structures, we have examined photochemical doping in solution. We have focused here on the simplest of the *n*-DNRs with more than one QD, the 2-DNR and its PL. Electrons in 2-DNRs are introduced through photoexcitation in the presence of a common hole scavenging molecule $Li[(Et)_3BH]$ ("superhydride") and oleylamine, which we collectively refer to as the "dopant". The use of superhydride[61,62] (sometimes in conjunction with oleylamine[63,64]) has been thoroughly described for the photochemical reduction of molecular precursors and QDs.

In core−shell QDs, the presence of an electron from photochemical doping will lead to the formation of the negative trion upon photoexciation, leading to nonradiative Auger recombination outcompeting PL.[62,65−69] Hence, a drastic reduction in the PL QY can be expected. When two different size CdSe QDs (emission peaks at 2.13 and 1.95 eV) mixed together in the same solution are photochemically doped, they exhibit identical proportional reductions in PL intensity as the dopant concentration increases (Supporting Information, Figure S4a−c). A mixture of CdSe/CdS core/shell QDs of two different emission colors also exhibits a similar response (Supporting Information, Figure S4d−f). In both cases, the PL intensity decreases monotonically with electron doping, and the yellow-to-red PL intensity ratio is approximately preserved, indicating a lack of significantly different reactivity with the dopant species or electron transfer between QDs in solution. This observation may be expected since the UV excitation is higher in energy than the band gap of both sizes of QDs, and the offset between dopant potential and QD valence band edge should be nearly independent of size. That is, there is no significant difference in the energy for hole scavenging from the smaller or the larger QDs, leading to electron occupation dependent on QD and dopant concentrations and not on QD size (i.e., the electron energy level position). Electron transfer between QDs is not significant, because of the low concentration that leads to long average distances between QDs.

Upon photochemical doping of the two-color emitting 2-DNRs (comparable in emission wavelengths to the control mixture of QDs discussed above), the PL QY *increases*, and a drastic change in color occurs. Prior to photochemical doping, the 2-DNRs exhibit a weak PL at 2.2 eV and a much stronger one at 2.0 eV. As shown in Figure 8a,b, increasing the dopant concentration leads to the 2.2 eV PL peak becoming much brighter, and the ratio of intensity between the 2.2 and 2.0 eV PL peaks ultimately inverts. This PL intensity inversion can be seen by eye through a striking change from an orange-red to yellow color (Figure 8c). Unlike the simple mixture of two different size QDs in solution, electron occupation in 2-DNRs is dependent on the constituent QD segment size. The UV excitation during the doping step can generate excitons in

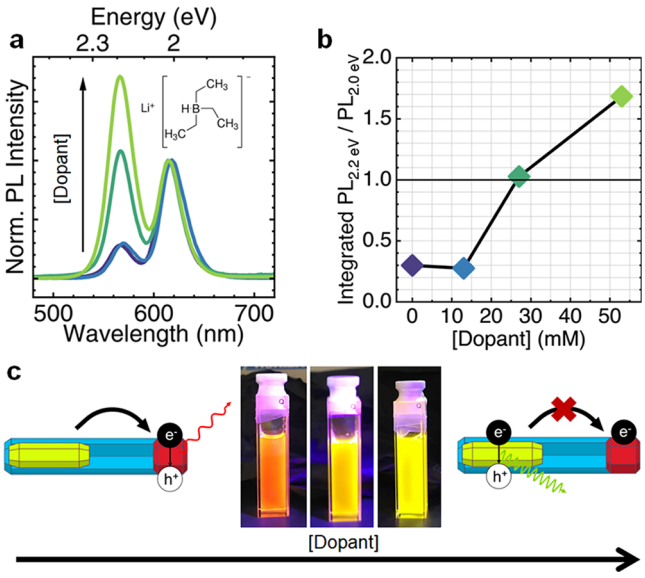

Figure 8. (a) Evolution of PL spectra of unidirectionally grown 2-DNRs upon photochemical doping with increasing $Li[(Et)_3BH]$ concentration from 0 to 53 mM, normalized to the intensity at the 2.0 eV peak. (b) Ratio of integrated PL intensities of the yellow and red PL peaks from the doped 2-DNRs obtained from Gaussian curve fitting. (c) Diagram illustrating doping-induced emission color change in 2-DNRs, and photographs of 2-DNR solutions under UV excitation with increasing concentration of the $Li[(Et)_3BH]$ dopant from left to right. In neutral particles, excitons are more likely to localize and recombine in the 2.0 eV emitting CdSe segment. Upon photochemical doping, the presence of an electron makes exciton localization in the 2.0 eV emitting segment less likely, leading to a greater probability of recombination in the 2.2 eV emitting CdSe segment.

either the smaller or the larger QD segment. The energetics of hole scavenging by the dopant will be similar to the core/shell QD case. However, unlike the simple mixture of core/shell QDs, coupling through the CdS rod should lead to the remaining electron preferentially occupying the lower energy conduction band edge of the less confined QD segment within the 2-DNR. This electron in the less confined QD segment can lead to preferential localization of the exciton in the other QD of the 2-DNR. Then, given the relatively large separation between QDs in 2-DNRs (∼10 nm) and given the expected long Auger lifetimes observed in quasi-type-II nanorod heterostructures,[70,71] radiative recombination probability in the more confined (2.2 eV emitting) CdSe segment increases while that of the less confined (2.0 eV emitting) CdSe decreases. This mechanism is illustrated in Figure 8c for before and after photochemical doping. The results of photochemical doping of 1-DNRs are shown in the Supporting Information, Figure S5, for additional comparison and indicate that the CdS rod "shell" alone does not lead to an unusual behavior.

Furthermore, the PL QY for emission at 2.2 eV can be expected to be higher after photochemical doping than before. Upon above-bandgap excitation of a neutral undoped 2-DNR, the lower conduction band edge position will drive electron relaxation or transfer to the red QD segment, decreasing the probability of higher energy radiative recombination in the yellow QD. The presence of an electron in the red QD segment will hinder exciton localization and electron transfer to it, effectively increasing the likelihood of radiative recombination in the yellow QD segment at the higher

https://doi.org/10.1021/jacs.3c14115
J. Am. Chem. Soc. 2024, 146, 9074−9083

emission energy of 2.2 eV. Indeed, the PL QY *increases* from about 3% to 9% from the pristine undoped condition to the highest concentration of the dopant. The unnormalized absolute intensities of the PL spectra are shown in the Supporting Information, Figure S5. Notably, this final value is similar to the PL QY measured at the 1-DNR stage of growth for this sample, suggesting that high PL QYs may be achieved with improved surface passivation, even in the presence of excess charge carriers in *n*-DNRs.

CONCLUSIONS

We have developed an approach to synthesize multidot CdSe/CdS *n*-DNRs with up to $n = 9$ CdSe QD segments. Their symmetry, length, and diameter can be varied through accessible synthesis conditions. In particular, we used the selection of phosphonic acid ligands, the seed-to-precursor ratio, and the reaction temperature to vary these three structural parameters. Both unidirectional and bidirectional growth modes, where each growth step can increment the number of QDs per rod by one or two for each cycle, respectively, have been achieved. For a model case of two-color emitting 2-DNRs, PL color change and a counterintuitive PL QY increase in response to electrons introduced through photochemical doping have been shown. In neutral 2-DNRs, lower energy emission from the larger QD segment is the more prominent feature. The presence of an electron blocks the interdot electron transfer within each *n*-DNR, leading to an enhancement of the higher energy PL. This ability to tune luminescence color through photochemical doping may be extended to electronic means as recently shown for colloidal QD molecules[72] and accelerate device applications. Whether through chemical, photochemical, or electrical means, exploring the charging limit of *n*-DNRs may lead to further interesting effects. The rich structural parameter space of *n*-DNRs that can be varied to control the size, shape, and interaction of QD segments and therefore their optical and electronic properties present many exciting avenues for future research. In addition to photochemical doping effects on multicolor emission initiated here, charge separation dynamics, single-[73] and two-photon[35,36,74] upconversion, and multicarrier processes are among many potentially interesting directions for *n*-DNRs.

ASSOCIATED CONTENT

Supporting Information

The Supporting Information is available free of charge at https://pubs.acs.org/doi/10.1021/jacs.3c14115.

Details of materials, synthesis, purification, photochemical doping and characterization; TEM micrographs with size histograms; PLE and absorptance spectra, and photochemical doping control data (PDF)

AUTHOR INFORMATION

Corresponding Author

Moonsub Shim − *Department of Materials Science and Engineering, University of Illinois at Urbana−Champaign, Urbana, Illinois 61801, United States;* orcid.org/0000-0001-7781-1029; Email: mshim@illinois.edu

Authors

Gryphon A. Drake − *Department of Materials Science and Engineering, University of Illinois at Urbana−Champaign, Urbana, Illinois 61801, United States;* orcid.org/0000-0002-4602-7562

Logan P. Keating − *Department of Materials Science and Engineering, University of Illinois at Urbana−Champaign, Urbana, Illinois 61801, United States;* orcid.org/0000-0002-1106-9658

Conan Huang − *Department of Materials Science and Engineering, University of Illinois at Urbana−Champaign, Urbana, Illinois 61801, United States*

Complete contact information is available at: https://pubs.acs.org/10.1021/jacs.3c14115

Notes

The authors declare no competing financial interest.

ACKNOWLEDGMENTS

Financial support from the U.S. National Science Foundation (Grant No. 2132538) is gratefully acknowledged. Experiments were carried out in part in the Frederick Seitz Materials Research Laboratory Central Research Facilities, University of Illinois.

REFERENCES

(1) Martynenko, I. V.; Litvin, A. P.; Purcell-Milton, F.; Baranov, A. V.; Fedorov, A. V.; Gun'Ko, Y. K. Application of Semiconductor Quantum Dots in Bioimaging and Biosensing. *J. Mater. Chem. B* **2017**, *5*, 6701−6727.

(2) Caruge, J.-M.; Halpert, J. E.; Wood, V. C.; cacute, V. B.; Bawendi, M. G. Colloidal Quantum−Dot Light-Emitting Diodes with Metal-Oxide Charge Transport Layers. *Nat. Photonics* **2008**, *2*, 247−250.

(3) Anikeeva, P.; Halpert, J. E.; Bawendi, M. G.; Bulović, V. Quantum Dot Light-Emitting Devices with Electroluminescence Tunable over the Entire Visible Spectrum. *Nano Lett.* **2009**, *9* (7), 2532−2536.

(4) Jiang, Y.; Cho, S. Y.; Shim, M. Light-Emitting Diodes of Colloidal Quantum Dots and Nanorod Heterostructures for Future Emissive Displays. *J. Mater. Chem. C* **2018**, *6*, 2618−2634.

(5) Choi, M. K.; Yang, J.; Hyeon, T.; Kim, D. H. Flexible Quantum Dot Light-Emitting Diodes for Next-Generation Displays. *npj Flexible Electron.* **2018**, *2*, 10.

(6) Bang, S. Y.; Suh, Y. H.; Fan, X. B.; Shin, D. W.; Lee, S.; Choi, H. W.; Lee, T. H.; Yang, J.; Zhan, S.; Harden-Chaters, W.; Samarakoon, C.; Occhipinti, L. G.; Han, S. D.; Jung, S. M.; Kim, J. M. Technology Progress on Quantum Dot Light-Emitting Diodes for Next-Generation Displays. *Nanoscale Horiz.* **2021**, *6*, 68−77.

(7) McDonald, S. A.; Konstantatos, G.; Zhang, S.; Cyr, P. W.; Klem, E. J. D.; Levina, L.; Sargent, E. H. Solution-Processed PbS Quantum Dot Infrared Photodetectors and Photovoltaics. *Nat. Mater.* **2005**, *4*, 138−142.

(8) Chuang, C.-H. M.; Brown, P. R.; Bulović, V.; Bawendi, M. G. Improved Performance and Stability in Quantum Dot Solar Cells through Band Alignment Engineering. *Nat. Mater.* **2014**, *13*, 796−801.

(9) Kirmani, A. R.; Luther, J. M.; Abolhasani, M.; Amassian, A. Colloidal Quantum Dot Photovoltaics: Current Progress and Path to Gigawatt Scale Enabled by Smart Manufacturing. *ACS Energy Lett.* **2020**, *5*, 3069−3100.

(10) Yang, Z.; Pelton, M.; Fedin, I.; Talapin, D. V.; Waks, E. A Room Temperature Continuous-Wave Nanolaser Using Colloidal Quantum Wells. *Nat. Commun.* **2017**, *8*, 143.

(11) Park, Y. S.; Roh, J.; Diroll, B. T.; Schaller, R. D.; Klimov, V. I. Colloidal Quantum Dot Lasers. *Nat. Rev. Mater.* **2021**, *6*, 382−401.

(12) Whitworth, G. L.; Dalmases, M.; Taghipour, N.; Konstantatos, G. Solution-Processed PbS Quantum Dot Infrared Laser with Room-

Temperature Tuneable Emission in the Optical Telecommunications Window. *Nat. Photonics* **2021**, *15*, 738−742.
(13) Santori, C. M.; Pelton, M.; Solomon, G. S.; Dale, Y.; Yamamoto, Y. Triggered Single Photons from a Quantum Dot. *Phys. Rev. Lett.* **2001**, *86* (8), 1502.
(14) Lin, X.; Dai, X.; Pu, C.; Deng, Y.; Niu, Y.; Tong, L.; Fang, W.; Jin, Y.; Peng, X. Electrically-Driven Single-Photon Sources Based on Colloidal Quantum Dots with Near-Optimal Antibunching at Room Temperature. *Nat. Commun.* **2017**, *8*, 1132.
(15) Drake, G. A.; Keating, L. P.; Shim, M. Design Principles of Colloidal Nanorod Heterostructures. *Chem. Rev.* **2023**, *123*, 3761−3789.
(16) Shieh, F.; Saunders, A. E.; Korgel, B. A. General Shape Control of Colloidal CdS, CdSe, CdTe Quantum Rods and Quantum Rod Heterostructures. *J. Phys. Chem. B* **2005**, *109*, 8538−8542.
(17) Carbone, L.; Cozzoli, P. D. Colloidal Heterostructured Nanocrystals: Synthesis and Growth Mechanisms. *Nano Today* **2010**, *5*, 449−493.
(18) Flanagan, J. C.; Keating, L. P.; Kalasad, M. N.; Shim, M. Extending the Spectral Range of Double-Heterojunction Nanorods by Cation Exchange-Induced Alloying. *Chem. Mater.* **2019**, *31*, 9307−9316.
(19) Smith, A. M.; Mohs, A. M.; Nie, S. Tuning the Optical and Electronic Properties of Colloidal Nanocrystals by Lattice Strain. *Nat. Nanotechnol.* **2009**, *4*, 56−63.
(20) Shim, M.; McDaniel, H.; Oh, N. Prospects for Strained Type-II Nanorod Heterostructures. *J. Phys. Chem. Lett.* **2011**, *2*, 2722−2727.
(21) Fan, F.; et al. Continuous-Wave Lasing in Colloidal Quantum Dot Solids Enabled by Facet-Selective Epitaxy. *Nature* **2017**, *544*, 75−79.
(22) Kim, D.; Shcherbakov-Wu, W.; Ha, S. K.; Lee, W. S.; Tisdale, W. A. Uniaxial Strain Engineering via Core Position Control in CdSe/CdS Core/Shell Nanorods and their Optical Response. *ACS Nano* **2022**, *16*, 14713−14722.
(23) Hu, J.; Li, L. S.; Yang, W.; Manna, L.; Wang, L. W.; Alivisatos, A. P. Linearly Polarized Emission from Colloidal Semiconductor Quantum Rods. *Science* **2001**, *292*, 2060−2063.
(24) Carbone, L.; et al. Synthesis and Micrometer-Scale Assembly of Colloidal CdSe/CdS Nanorods Prepared by a Seeded Growth Approach. *Nano Lett.* **2007**, *7*, 2942−2950.
(25) Sitt, A.; Salant, A.; Menagen, G.; Banin, U. Highly Emissive Nano Rod-In-Rod Heterostructures with Strong Linear Polarization. *Nano Lett.* **2011**, *11*, 2054−2060.
(26) Nam, S.; Oh, N.; Zhai, Y.; Shim, M. High Efficiency and Optical Anisotropy in Double-Heterojunction Nanorod Light-Emitting Diodes. *ACS Nano* **2015**, *9*, 878−885.
(27) Kim, W. D.; Kim, D.; Yoon, D. E.; Lee, H.; Lim, J.; Bae, W. K.; Lee, D. C. Pushing the Efficiency Envelope for Semiconductor Nanocrystal-Based Electroluminescence Devices Using Anisotropic Nanocrystals. *Chem. Mater.* **2019**, *31*, 3066−3082.
(28) Bai, X.; Li, H.; Peng, Y.; Zhang, G.; Yang, C.; Guo, W.; Han, X.; Li, J.; Chen, R.; Qin, C.; Hu, J.; Yang, G.; Zhong, H.; Xiao, L.; Jia, S. Role of Aspect Ratio in the Photoluminescence of Single CdSe/CdS Dot-in-Rods. *J. Phys. Chem. C* **2022**, *126*, 2699−2707.
(29) Kumar, S.; Jones, M.; Lo, S. S.; Scholes, G. D. Nanorod Heterostructures Showing Photoinduced Charge Separation. *Small* **2007**, *3*, 1633−1639.
(30) Kirsanova, M.; Nemchinov, A.; Hewa-Kasakarage, N. N.; Schmall, N.; Zamkov, M. Synthesis of ZnSe/CdS/ZnSe Nanobarbells Showing Photoinduced Charge Separation. *Chem. Mater.* **2009**, *21*, 4305−4309.
(31) McDaniel, H.; Pelton, M.; Oh, N.; Shim, M. Effects of Lattice Strain and Band Offset on Electron Transfer Rates in Type-II Nanorod Heterostructures. *J. Phys. Chem. Lett.* **2012**, *3*, 1094−1098.
(32) Grennell, A. N.; Utterback, J. K.; Pearce, O. M.; Wilker, M. B.; Dukovic, G. Relationships between Exciton Dissociation and Slow Recombination within ZnSe/CdS and CdSe/CdS Dot-in-Rod Heterostructures. *Nano Lett.* **2017**, *17*, 3764−3774.
(33) Bera, R.; Dutta, A.; Kundu, S.; Polshettiwar, V.; Patra, A. Design of a CdS/CdSe Heterostructure for Efficient H_2 Generation and Photovoltaic Applications. *J. Phys. Chem. C* **2018**, *122*, 12158−12167.
(34) Lee, S.; Flanagan, J. C.; Kim, J.; Yun, A. J.; Lee, B.; Shim, M.; Park, B. Efficient Type-II Heterojunction Nanorod Sensitized Solar Cells Realized by Controlled Synthesis of Core/Patchy-Shell Structure and CdS Cosensitization. *ACS Appl. Mater. Interfaces* **2019**, *11*, 19104−19114.
(35) Chen, E. Y.; Li, Z.; Milleville, C. C.; Lennon, K. R.; Zide, J. M.; Doty, M. F. CdSe(Te)/CdS/CdSe Rods Versus CdTe/CdS/CdSe Spheres: Morphology-Dependent Carrier Dynamics for Photon upconversion. *IEEE J. Photovoltaics* **2018**, *8*, 746−751.
(36) Milleville, C. C.; Chen, E. Y.; Lennon, K. R.; Cleveland, J. M.; Kumar, A.; Zhang, J.; Bork, J. A.; Tessier, A.; Lebeau, J. M.; Chase, D. B.; Zide, J. M.; Doty, M. F. Engineering Efficient Photon Upconversion in Semiconductor Heterostructures. *ACS Nano* **2019**, *13*, 489−497.
(37) Oh, N.; et al. Double-Heterojunction Nanorod Light-Responsive LEDs for Display Applications. *Science* **2017**, *355*, 616−619.
(38) Cui, J.; Panfil, Y. E.; Koley, S.; Shamalia, D.; Waiskopf, N.; Remennik, S.; Popov, I.; Oded, M.; Banin, U. Colloidal Quantum Dot Molecules Manifesting Quantum Coupling at Room Temperature. *Nat. Commun.* **2019**, *10*, 5401.
(39) Cui, J.; Koley, S.; Panfil, Y. E.; Levi, A.; Waiskopf, N.; Remennik, S.; Oded, M.; Banin, U. Semiconductor Bow-Tie Nanoantenna from Coupled Colloidal Quantum Dot Molecules. *Angew. Chem.* **2021**, *133*, 14588−14593.
(40) Alivisatos, A. P.; Johnsson, K. P.; Peng, X.; Wilson, T. E.; Loweth, C. J.; Bruchez, M. P.; Schultz, P. G. Organization of Nanocrystal Molecules Using DNA. *Nature* **1996**, *382*, 609−611.
(41) Tikhomirov, G.; Hoogland, S.; Lee, P. E.; Fischer, A.; Sargent, E. H.; Kelley, S. O. DNA-based Programming of Quantum Dot Valency, Self-Assembly and Luminescence. *Nat. Nanotechnol.* **2011**, *6*, 485−490.
(42) Coopersmith, K.; Han, H.; Maye, M. M. Stepwise Assembly and Characterization of DNA Linked Two-Color Quantum Dot Clusters. *Langmuir* **2015**, *31*, 7463−7471.
(43) Drake, G. A.; Flanagan, J. C.; Shim, M. Highly Luminescent Double-Heterojunction Nanorods. *J. Chem. Phys.* **2019**, *151*, No. 134706.
(44) Alferov, Z. I. The Double Heterostructure. *International Journal of Modern Physics B* **2002**, *16*, 647−675.
(45) Faist, J.; Capasso, F.; Sivco, D. L.; Sirtori, C.; Hutchinson, A. L.; Cho, A. Y. Quantum Cascade Laser. *Science* **1994**, *264*, 553−556.
(46) Peng, X.; Schlamp, M. C.; Kadavanich, A. V.; Alivisatos, A. P. Epitaxial Growth of Highly Luminescent CdSe/CdS Core/Shell Nanocrystals with Photostability and Electronic Accessibility. *J. Am. Chem. Soc.* **1997**, *119*, 7019−7029.
(47) Chen, O.; Zhao, J.; Chauhan, V. P.; Cui, J.; Wong, C.; Harris, D. K.; Wei, H.; Han, H. S.; Fukumura, D.; Jain, R. K.; Bawendi, M. G. Compact High-Quality CdSe-CdS Core-Shell Nanocrystals with Narrow Emission Linewidths and Suppressed Blinking. *Nat. Mater.* **2013**, *12*, 445−451.
(48) Coropceanu, I.; Rossinelli, A.; Caram, J. R.; Freyria, F. S.; Bawendi, M. G. Slow-Injection Growth of Seeded CdSe/CdS Nanorods with Unity Fluorescence Quantum Yield and Complete Shell to Core Energy Transfer. *ACS Nano* **2016**, *10*, 3295−3301.
(49) Kim, D.; Lee, Y. K.; Lee, D.; Kim, W. D.; Bae, W. K.; Lee, D. C. Colloidal Dual-Diameter and Core-Position-Controlled Core/Shell Cadmium Chalcogenide Nanorods. *ACS Nano* **2017**, *11*, 12461−12472.
(50) Enright, M. J.; Sarsito, H.; Cossairt, B. M. Kinetically Controlled Assembly of Cadmium Chalcogenide Nanorods and Nanorod Heterostructures. *Mater. Chem. Front.* **2018**, *2*, 1296−1305.
(51) Oh, N.; Nam, S.; Zhai, Y.; Deshpande, K.; Trefonas, P.; Shim, M. Double-Heterojunction Nanorods. *Nat. Commun.* **2014**, *5*, 3642.

https://doi.org/10.1021/jacs.3c14115
J. Am. Chem. Soc. 2024, 146, 9074−9083

(52) Demortière, A.; Leonard, D. N.; Petkov, V.; Chapman, K.; Chattopadhyay, S.; She, C.; Cullen, D. A.; Shibata, T.; Pelton, M.; Shevchenko, E. V. Strain-Driven Stacking Faults in CdSe/CdS Core/Shell Nanorods. *J. Phys. Chem. Lett.* **2018**, *9*, 1900−1906.
(53) Wu, K.; Hill, L. J.; Chen, J.; McBride, J. R.; Pavlopolous, N. G.; Richey, N. E.; Pyun, J.; Lian, T. Universal Length Dependence of Rod-to-Seed Exciton Localization Efficiency in Type I and Quasi-Type II CdSe@CdS Nanorods. *ACS Nano* **2015**, *9*, 4591−4599.
(54) Diroll, B. T.; Greybush, N. J.; Kagan, C. R.; Murray, C. B. Smectic Nanorod Superlattices Assembled on Liquid Subphases: Structure, Orientation, Defects, and Optical Polarization. *Chem. Mater.* **2015**, *27*, 2998−3008.
(55) Rice, K. P.; Saunders, A. E.; Stoykovich, M. P. Seed-Mediated Growth of Shape-Controlled Wurtzite CdSe Nanocrystals: Platelets, Cubes, and Rods. *J. Am. Chem. Soc.* **2013**, *135*, 6669−6676.
(56) Li, H.; Geelhaar, L.; Riechert, H.; Draxl, C. Computing Equilibrium Shapes of Wurtzite Crystals: The Example of GaN. *Phys. Rev. Lett.* **2015**, *115*, No. 085503.
(57) Bladt, E.; Van Dijk-Moes, R. J.; Peters, J.; Montanarella, F.; De Mello Donega, C.; Vanmaekelbergh, D.; Bals, S. Atomic Structure of Wurtzite CdSe (Core)/CdS (Giant Shell) Nanobullets Related to Epitaxy and Growth. *J. Am. Chem. Soc.* **2016**, *138*, 14288−14293.
(58) Peng, Z. A.; Peng, X. Nearly Monodisperse and Shape-Controlled CdSe Nanocrystals via Alternative Routes: Nucleation and Growth. *J. Am. Chem. Soc.* **2002**, *124*, 3343−3353 PMID: 11916419.
(59) Talapin, D. V.; Nelson, J. H.; Shevchenko, E. V.; Aloni, S.; Sadtler, B.; Alivisatos, A. P. Seeded Growth of Highly Luminescent CdSe/CdS Nanoheterostructures with Rod and Tetrapod Morphologies. *Nano Lett.* **2007**, *7*, 2951−2959.
(60) Manna, L.; Wang, L. W.; Cingolani, R.; Alivisatos, A. P. First-Principles Modeling of Unpassivated and Surfactant-Passivated Bulk Facets of Wurtzite CdSe: A Model System for Studying the Anisotropic Growth of CdSe Nanocrystals. *J. Phys. Chem. B* **2005**, *109*, 6183−6192.
(61) Rinehart, J. D.; Schimpf, A. M.; Weaver, A. L.; Cohn, A. W.; Gamelin, D. R. Photochemical Electronic Doping of Colloidal CdSe Nanocrystals. *J. Am. Chem. Soc.* **2013**, *135*, 18782−18785.
(62) Hou, X.; Kang, J.; Qin, H.; Chen, X.; Ma, J.; Zhou, J.; Chen, L.; Wang, L.; Wang, L. W.; Peng, X. Engineering Auger Recombination in Colloidal Quantum Dots via Dielectric Screening. *Nat. Commun.* **2019**, *10*, 1750.
(63) Zhang, J.; Jin, S.; Fry, H. C.; Peng, S.; Shevchenko, E.; Wiederrecht, G. P.; Rajh, T. Synthesis and Characterization of Wurtzite ZnTe Nanorods with Controllable Aspect Ratios. *J. Am. Chem. Soc.* **2011**, *133*, 15324−15327.
(64) Wang, F.; Javaid, S.; Chen, W.; Wang, A.; Buntine, M. A.; Jia, G. Synthesis of Atomically Thin CdTe Nanoplatelets by Using Polytelluride Tellurium Precursors. *Aust. J. Chem.* **2021**, *74*, 179−185.
(65) Robel, I.; Gresback, R.; Kortshagen, U.; Schaller, R. D.; Klimov, V. I. Universal Size-Dependent Trend in Auger Recombination in Direct-Gap and Indirect-Gap Semiconductor Nanocrystals. *Phys. Rev. Lett.* **2009**, *102*, No. 177404.
(66) Cohn, A. W.; Rinehart, J. D.; Schimpf, A. M.; Weaver, A. L.; Gamelin, D. R. Size Dependence of Negative Trion Auger Recombination in Photodoped CdSe Nanocrystals. *Nano Lett.* **2014**, *14*, 353−358.
(67) Park, Y. S.; Bae, W. K.; Padilha, L. A.; Pietryga, J. M.; Klimov, V. I. Effect of the Core/Shell Interface on Auger Recombination Evaluated by Single-Quantum-Dot Spectroscopy. *Nano Lett.* **2014**, *14*, 396−402.
(68) Gao, F.; Bajwa, P.; Nguyen, A.; Heyes, C. D. Shell-Dependent Photoluminescence Studies Provide Mechanistic Insights into the Off-Grey-On Transitions of Blinking Quantum Dots. *ACS Nano* **2017**, *11*, 2905−2916.
(69) Wu, K.; Lim, J.; Klimov, V. I. Superposition Principle in Auger Recombination of Charged and Neutral Multicarrier States in Semiconductor Quantum Dots. *ACS Nano* **2017**, *11*, 8437−8447.
(70) Zavelani-Rossi, M.; Lupo, M. G.; Tassone, F.; Manna, L.; Lanzani, G. Suppression of Biexciton Auger Recombination in CdSe/CdS Dot/Rods: Role of the Electronic Structure in the Carrier Dynamics. *Nano Lett.* **2010**, *10*, 3142−3150.
(71) Rabouw, F. T.; Lunnemann, P.; Van Dijk-Moes, R. J.; Frimmer, M.; Pietra, F.; Koenderink, A. F.; Vanmaekelbergh, D. Reduced Auger Recombination in Single CdSe/CdS Nanorods by One-Dimensional Electron Delocalization. *Nano Lett.* **2013**, *13*, 4884−4892.
(72) Ossia, Y.; Levi, A.; Panfil, Y. E.; Koley, S.; Scharf, E.; Chefetz, N.; Remennik, S.; Vakahi, A.; Banin, U. Electric-Field-Induced Colour Switching in Colloidal Quantum Dot Molecules at Room Temperature. *Nat. Mater.* **2023**, *22*, 1210−1217.
(73) Ye, Z.; Lin, X.; Wang, N.; Zhou, J.; Zhu, M.; Qin, H.; Peng, X. Phonon-Assisted Up-Conversion Photoluminescence of Quantum Dots. *Nat. Commun.* **2021**, *12*, 4283.
(74) Deutsch, Z.; Neeman, L.; Oron, D. Luminescence Upconversion in Colloidal Double Quantum Dots. *Nat. Nanotechnol.* **2013**, *8*, 649−653.

https://doi.org/10.1021/jacs.3c14115
J. Am. Chem. Soc. 2024, 146, 9074−9083